Journal of
Materials Chemistry A

PAPER

View Article Online
View Journal | View Issue

Check for updates

Cite this: *J. Mater. Chem. A*, 2019, **7**, 1749

Electrolyte regulation enhances the stability of Prussian blue analogues in aqueous Na-ion storage†

Tielei Shao,[a] Chang Li,[a] Chunyi Liu,[a] Wenjun Deng,[a] Weijian Wang,[a] Mianqi Xue[b] and Rui Li*[a]

Received 11th November 2018
Accepted 13th December 2018

DOI: 10.1039/c8ta10860a

rsc.li/materials-a

In this study, we employed $Na_2CoFe(CN)_6$ (CoHCF), which was synthesized by a commonly used co-precipitation method, as the cathode material for aqueous sodium-ion batteries (ASIBs). By adding an electrolyte additive (1 wt% $CoSO_4$) in the aqueous electrolyte (1 M Na_2SO_4), the framework structures were stabilized and the cycle stability was significantly improved (100% capacity retention at a current density of 2C (1C = 120 mA g^{-1})) after 100 cycles without affecting the initial reversible capacity. Long-term cycle tests (2000 cycles) at current densities of 10C and 20C were also performed and indicated similar improvement. The XRD, FT-IR, and ICP-AES results demonstrated that better structure maintenance of the CoHCF framework can be realized when Co^{2+} ions were added. We suggest that such a simple method can be extended to all PBAs to improve the overall performance of SIBs effectively.

Introduction

Lithium-ion batteries (LIBs) are currently the most important energy storage devices for lightweight, flexible wearable devices and electric vehicles.[1–3] However, the uneven distribution and low abundance of lithium in the Earth's crust (accounting for 0.0017% compared to 2.36% of sodium and 2.09% of potassium)[4] limit their large-scale applications.[5,6] Aqueous sodium-ion batteries (ASIBs) appear to be a more attractive candidate and have attracted intense interest for large-scale electric energy storage because of their low cost, high safety, and environmental friendliness.[7–9] Nevertheless, due to the narrow electrochemical window of aqueous electrolytes, it is challenging to find suitable cathode materials for ASIBs, which are supposed to possess suitable voltage platforms, chemical stability in aqueous electrolytes, and large channels to allow fast Na^+ ion transport.

Recently, Prussian blue analogues (PBAs) have been widely investigated as the cathode for SIBs[10–13] because their open frameworks can provide large ionic channels and Na-insertion sites. The chemical formula of the experimentally synthesized PBAs is generally presented as $A_{2-x}M_1[M_2(CN)_6]_{1-y}\cdot\square_y\cdot nH_2O$ ($0 < x < 2$, $0 < y < 1$), where A is an alkali metal ion such as Na^+ and K^+, M_1 and M_2 are transition metals located at octahedral sites, which are linked to N and C through coordination bonds, respectively, and $\square$ stands for hexacyanometallate anion $[M_2(CN)_6]$ vacancies, which can reduce the Na content by introducing more crystal water to occupy the interstitial spaces.[14] In particular, the random distribution of vacancies can make the PBA frameworks fragile and vulnerable to collapse, which can lead to structural instability during the charge–discharge process and poor cycle life.[15] In addition, when N-coordinated M_1 is Co/Mn, the weak N-coordinated crystal field results in structural distortions, which cause phase change from a cubic lattice to a rhombohedral one.[16,17] Cui and co-workers conducted a systematic study on this issue by examining the correlation between the electrochemical behaviours and structural features of MnFe–PBA, CoFe–PBA, and MnCoFe–PBA materials in aqueous electrolytes.[18] The lattice distortion affects cycle stability because it may cause the cleavage of the M_1–N≡C–Fe bridge and the dissolution of transition metal ions in the framework, especially in an aqueous electrolyte. It should be noted that the gradual dissolution of the electrode material in an aqueous solution is also a key factor causing decrease in cycle stability, which is always ignored. The theoretical capacity of CoHCF is ~170 mA h g^{-1}. However, it is difficult for all the theoretical capacity to be fully used, especially in an aqueous electrolyte, due to the reasons mentioned above. Generally, optimizing synthesis conditions to obtain PBAs with high crystallinity and less defects/vacancies is an effective method for improving the capacity and cycle stability of PBAs. To date, most studies on PBAs have focused on the optimization of materials[12,15,19] or electrodes[20,21] themselves.

In this study, we proposed a novel idea to improve the cycle stability of PBAs as a cathode material for aqueous SIBs by

---

[a] *School of Advanced Materials, Peking University Shenzhen Graduate School, Shenzhen 518055, China. E-mail: lirui@pkusz.edu.cn*

[b] *Technical Institute of Physics and Chemistry, Chinese Academy of Sciences, Beijing, 100190, China*

† Electronic supplementary information (ESI) available. See DOI: 10.1039/c8ta10860a

regulating the electrolyte. The as-prepared $Na_2CoFe(CN)_6$ (CoHCF) was synthesized by a reported facile citrate-assisted co-precipitation method to control crystallization,[15] which exhibited reversible capacities of 110.8 mA h g^{-1} and 61 mA h g^{-1} at current densities of 2C and 20C (1C = 120 mA g^{-1}), respectively. Here, we introduced a regulated electrolyte with 1 wt% $CoSO_4$ as an additive in 1 M Na_2SO_4; compared to the samples in blank electrolyte 1 M Na_2SO_4 (CoHCF-B), CoHCF working in such regulated Co-added electrolyte (CoHCF-R) shows significant improvement in cycle stability. Furthermore, the framework structure changes in the electrodes have been analysed by X-ray diffraction (XRD), Fourier transform infrared spectroscopy (FT-IR) and inductively coupled plasma-atomic emission spectrometry (ICP-AES) after cycling, which indicate that the addition of Co^{2+} ions can be helpful to restrain the framework structure of CoHCF from degeneration and inhibit dissolution during cycling. This study is expected to provide guidance for improving the cycling performance of PBA cathodes in ASIBs.

Experimental section

Synthesis of cubic $Na_2CoFe(CN)_6$

All chemicals were obtained from Sinopharm Chemical Reagent Co. Ltd (China) and were used without further treatment. The $Na_2CoFe(CN)_6$ nanocubes were synthesized *via* a simple modified co-precipitation method. Typically, 5 mmol of sodium ferrocyanide was dissolved into 200 mL deionized water to obtain solution A, and 5 mmol of cobalt chloride and 30 mmol of sodium citrate were dissolved in 200 mL deionized water to obtain solution B; then, the two solutions were directly mixed and constantly stirred at room temperature. After 24 h, the obtained green precipitate was collected by centrifugation and washed by deionized water and ethanol three times. Finally, the sample was dried in a vacuum oven at 100 °C for 12 h.

Material characterizations

The crystal structures of the materials were measured by an X-ray diffractometer (XRD, Bruker D8 Advance) with Cu Kα radiation ($\lambda = 1.5416$ Å). The chemical composition of CoHCF and Fe content in the electrolytes were measured by elemental analyzer and inductively coupled plasma-atomic emission spectroscopy (ICP-AES, HORIBA JOBINYVON JY2000-2), respectively. The morphological and elemental mapping studies of $Na_2CoFe(CN)_6$ were performed by scanning electron microscopy (SEM, Carl Zeiss Supra 55) with an Oxford AZtec energy dispersive spectrometer. The changes in element valence state during charge and discharge were characterized by an X-ray Photoelectron Spectrometer (Thermo Fisher ESCALAB 250Xi). The FT-IR spectra of CoHCF electrodes were measured by an infrared spectrometer (Frontier, PerkinElmer).

Preparation of the electrodes and electrochemical tests

All the electrochemical properties of the $Na_2CoFe(CN)_6$ samples were studied at room temperature using a half-cell configuration (three-electrode system), and all electrodes were fabricated under room temperature and standard atmospheric pressure. The CoHCF electrodes were fabricated into films with thickness of 0.2–0.3 mm and areal density ~9.1 mg cm^{-2}. They were made up of a mixture of active material, carbon black, and poly(tetrafluoroethylene) (PTFE) in a weight ratio of 7 : 2 : 1 and then pressed onto titanium mesh. The mass loading of CoHCF electrode is ~6.4 mg cm^{-2}. Considering the capacity, wide potential window, conveniences and stability of activated carbon (AC), the counter electrode was prepared in the same way as the above working electrode with the mixture of AC, acetylene black and PTFE at a weight ratio of 8 : 1 : 1. The P/N ratio is 1 : 1.3 in this study. Using 1 mol L^{-1} Na_2SO_4 aqueous solution as electrolyte for the half-cell test, the contents of added electrolyte additive $CoSO_4$ in CoHCF-B and CoHCF-R were 0 wt% and 1 wt%, respectively, and a saturated calomel electrode (SCE) was used as the reference electrode. The potential of the three-electrode system was measured between the CoHCF electrode and reference electrode. Cyclic voltammetry (CV, 1 mV s^{-1}) tests were performed on an electrochemical workstation (CHI660D). Considering the discharge capacity of as-prepared CoHCF, C-rate is employed as 1C = 120 mA g^{-1}. The battery tests were carried out at various current densities by using a battery test system (LAND CT2001A). Electrochemical impedance spectroscopy (EIS) was carried out with 5 mV amplitude in the frequency range between 0.01 Hz and 100 kHz using a CHI604E electrochemical workstation.

Results and discussion

Scheme 1 shows a schematic of the growth process of $Na_2CoFe(CN)_6$ (CoHCF) nanocubes. Co^{2+} ions are first coordinated with citrate ions to form a cobalt citrate chelate (solution B) and then co-precipitated with hexacyanoferrate ions (solution A) in aqueous solution with constant stirring to ensure that the ingredients are homogeneous throughout the solution. Due to the very strong complex ability of citrate ions, Co^{2+} ions are slowly released from the cobalt citrate chelate, allowing slow nucleation and controllable crystal growth to suppress the structural defects.

On the basis of the elemental analysis for C, N, and H and inductively coupled plasma atomic emission spectroscopy (ICP-AES) for Na, Co and Fe (as shown in Table S1†), the quantitative chemical composition of the as-prepared $Na_2CoFe(CN)_6$ material can be expressed as $Na_{1.51}Co[Fe(CN)_6]_{0.85}\cdot_{0.15}\cdot 2.72H_2O$ (stands for the $Fe(CN)_6$ vacancies). Moreover, 15% of $Fe(CN)_6$

Scheme 1 Schematic of the growth process of $Na_2CoFe(CN)_6$ nanocubes.

defect content results in a relatively low Na content and theoretical capacity (~150 mA h g^{-1}). Of course, adjusting the concentration of the solution A/B and the ratio of sodium citrate can control the structure of the sample and reduce the content of defects. It has also been reported that with the assistance of ascorbic acid and N_2 atmosphere, which can prevent the oxidation of $Fe^{2+}/[Fe^{II}(CN)_6]^{4-}$ to $Fe^{3+}/[Fe^{III}(CN)_6]^{3-}$,[22] and adding Na salt during the synthesis process, which can increase the Na content, high-quality samples can be obtained.[23]

Fig. 1 shows the crystalline structure and morphological features of the as-prepared CoHCF material. The wide-angle XRD pattern (Fig. 1a) shows sharp peaks and no other miscellaneous peaks, indicating that the samples are well crystallized and pure. It can be observed that the diffraction peaks of all samples shift slightly toward lower diffraction angles, implying a larger lattice parameter, which is beneficial to the sodium ion transport. Compared with the cubic phase, the (220), (420), (440) and (620) diffraction peaks split into two diffraction peaks with almost equal intensities, which indicates the rhombohedral distortion from a traditional face-centred cubic structure. In addition, the sodium content is related to the intensity of the split peaks.[24] Fig. 1b shows the crystal structure of these PBAs in which octahedrally coordinated transition metal hexacyanides form an open framework with 6-fold, nitrogen-coordinated transition metals.[25] The interstitial "A sites" are occupied by hydrated alkaline ions or zeolitic water; R sites and P sites are transition metal ions (Fe and Co in this study). The SEM image in Fig. 1c reveals that the as-prepared CoHCF sample contains well-dispersed nanocubes (~500 nm) with sharp edges and flat surfaces. Energy dispersive spectroscopy (EDS) mapping images (Fig. 1d and e) confirm the uniform distribution of Na, Co, Fe, C, N, and O in the $Na_2CoFe(CN)_6$ sample, and the excess carbon distribution originates from the conductive adhesive substrate used in the test.

The electrochemical behaviours of CoHCF are assessed by CV and galvanostatic measurements in a three-electrode cell system with a saturated calomel electrode (SCE) as the reference electrode and an active carbon electrode as the counter electrode. As shown in Fig. 2a, the CV curve of CoHCF shows two pairs of oxidation-reduction peaks located at 0.3–0.5 V (*vs.* SCE) and 0.8–1.0 V (*vs.* SCE) at a scan rate of 1 mV s^{-1} in 1.0 mol L^{-1} Na_2SO_4 aqueous electrolyte, which are assigned to the nitrogen-coordinated couple (Co^{III}/Co^{II}–N) and carbon-coordinated couple (Fe^{III}/Fe^{II}–C), respectively.[26] The charge/discharge profiles of CoHCF cathode at 2C are shown in Fig. 2b. The initial charge/discharge capacities are 131.1 and 110.8 mA h g^{-1}, respectively. All the curves exhibit two separate potential plateaus, corresponding to the two-electron redox reactions in CV curve, and indicate the 2-Na reaction mechanism; the equations can be written as follows:

$$Na_2Co^{II}[Fe^{II}(CN)_6] \rightarrow Na^+ + e^- + NaCo^{III}[Fe^{II}(CN)_6] \quad (1)$$

$$NaCo^{III}[Fe^{II}(CN)_6] \rightarrow Na^+ + e^- + Co^{III}[Fe^{III}(CN)_6] \quad (2)$$

X-ray photoelectron spectra (XPS) are obtained to further verify the valence change of the transition metal ions on three states during the cycle (Fig. S1 and S2†). The Na 1s spectra in Fig. S1b† demonstrate the extraction/insertion of Na^+ ions after

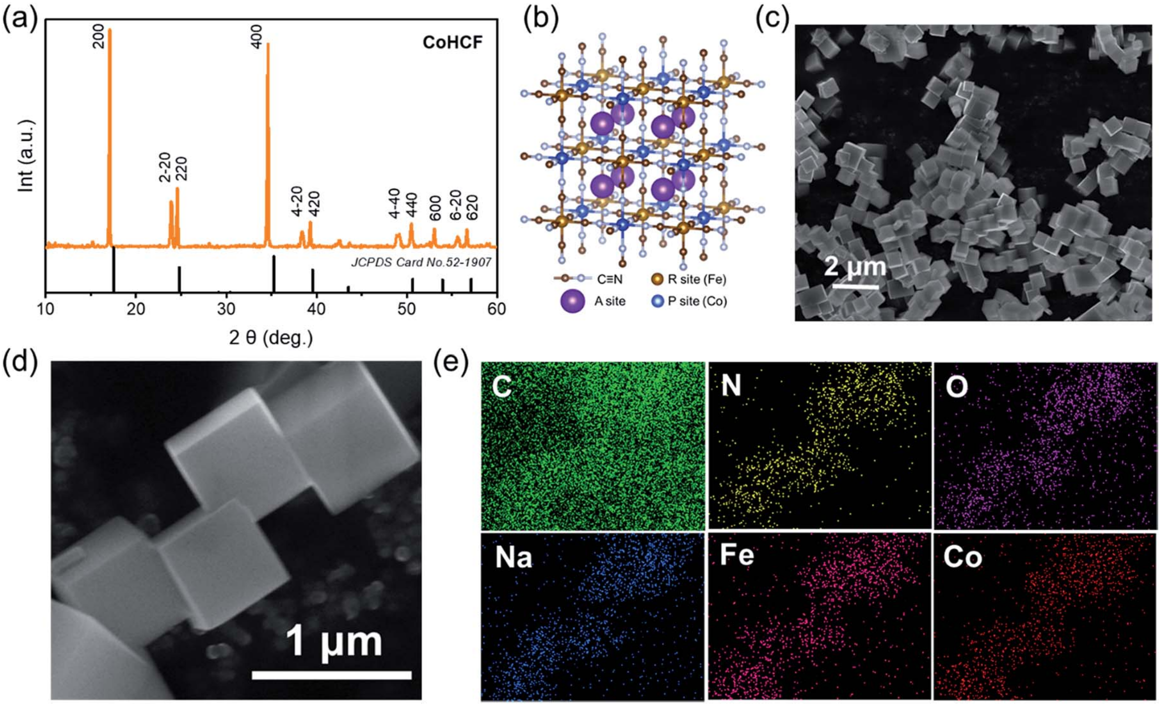

Fig. 1 Characterization of the as-prepared CoHCF sample. (a) XRD pattern, (b) crystal structure, (c) SEM image, and (d and e) energy dispersive spectroscopy mapping images.

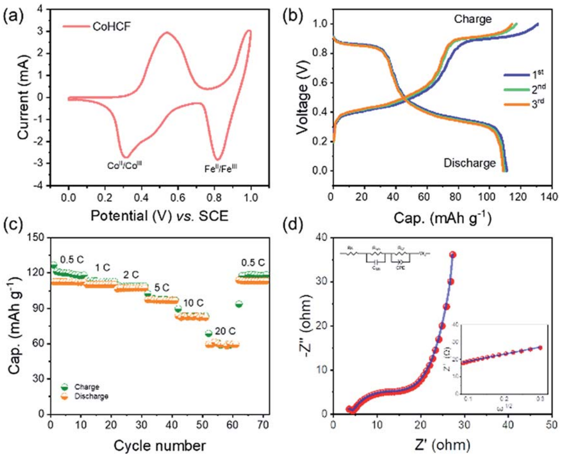

Fig. 2 Electrochemical performances of the as-prepared $Na_2CoFe(CN)_6$. (a) The cyclic voltammogram (CV) curve of CoHCF at a scan rate of 1 mV s^{-1} with a potential window between 0 and 1 V (*vs.* SCE). (b) Charge and discharge profiles of CoHCF electrode at a current density of 2C (1C = 120 mA g^{-1}). (c) Specific capacities of CoHCF at various current densities, and (d) EIS spectra for CoHCF electrode; the insets are the equivalent electric circuit and corresponding linear fitting curve.

being fully charged to 1 V and discharged to 0 V. The Fe 2p and Co 2p spectra in three states (Fig. S2†) show the processes of $Co^{II}/Co^{III}/Co^{II}$ and $Fe^{II}/Fe^{III}/Fe^{II}$, which can clarify the reaction mechanism.

Fig. 2c exhibits that the reversible capacities are 112, 110, 107, 97, 84 and 61 mA h g^{-1} at current densities of 0.5C, 1C, 2C, 5C, 10C and 20C (1C = 120 mA g^{-1}), respectively. More than 54% capacity utilization is maintained under high current density of 20C compared with that under 0.5C; this can be ascribed to large Na-ion channels and high surface contribution of electron conduction.[27,28] The Na^+ ion diffusivity (1.72×10^{-14} cm^2 s^{-1}) of CoHCF has been calculated based on the result of electrochemical impedance spectroscopy (EIS) (Fig. 2d, please see the ESI† for calculation details), which is close to those of other reported SIB cathode materials.[29–31]

Fig. 3 shows the cycle performances of CoHCF-B and CoHCF-R, and the contents of added electrolyte additive $CoSO_4$ in CoHCF-B and CoHCF-R are 0 wt% and 1 wt%, respectively. As shown in Fig. 3a, the reversible capacity of CoHCF-B decreases rapidly from 110.8 to 79.5 mA h g^{-1} over 100 cycles at a current density of 2C. Interestingly, the CoHCF-R sample shows perfect cycle performance with reversible capacity retention of 100% (~115 mA h g^{-1}) after 100 cycles. The slight increase/decrease in capacity during the cycling process may be caused by temperature changes in the surrounding environment (diurnal temperature fluctuation). Similarly, the long-term cycle performances shown in Fig. 3c indicate that the reversible capacity of CoHCF-B declined sharply from 99.2 to 20.6 mA h g^{-1} after 2000 cycles at a current density of 10C, whereas the CoHCF-R sample still retains a reversible capacity of 66.3 mA h g^{-1}, which is more than three times that of CoHCF-B. We also performed long-term cycle tests under larger current density of 20C, as shown in Fig. S4;† the CoHCF-R sample still showed better cycle performance than CoHCF-B. The statistics of reversible capacities of the two samples before and after 100/2000/2000 cycles at different current densities are shown in Fig. 3b; the results show that the capacity retentions increase from 71.5%, 20.8%, and 55.7% to 100%, 69.2%, and 75.6% after the addition of the electrolyte additive $CoSO_4$. The excellent cycle performance of CoHCF-R is superior to those of most of the previously reported PBAs and other materials in SIBs.[11,16,19,24,32–37]

The SEM images of CoHCF-B before and after 100 cycles are shown in Fig. S4,† which show no clear change in the morphology of CoHCF nanocubes after cycling. To further examine the changes in the internal framework structure after adding the additives of Co^{2+} ions, which improved the cycle stability of CoHCF, XRD measurements of the electrodes of CoHCF-B and CoHCF-R before and after 100 cycles were obtained. As shown in Fig. 4, the XRD patterns of CoHCF-B and CoHCF-R after cycling were obtained when the half-cell test system returned to the stable open circuit voltage (0.3 V for CoHCF-B and 0.35 V for CoHCF-R) from a full-charged state (1 V). After cycling, both the samples show clear change: all diffraction peaks slightly shift to higher angles, and the (2–20) and (220) diffraction peaks at $2\theta \approx 25°$ decrease in intensity and then integrate into one single (220) peak, corresponding to the reversible structural phase transition of the rhombohedral structure to face-centred-cubic, which has been reported many times.[16,17] The phase transition also occurred at diffraction peaks of $2\theta \approx 35°$ and 40° (corresponding to (400) and (420)). For both samples after 100 cycles, the only difference is the intensities of splitting at peaks of $2\theta \approx 25°$ and 35°, which can be seen from the illustration on the right side; it is related to the sodium content in the framework structure,[24] and no other apparent structural differences are found. This means that the relative sodium content in CoHCF-R is higher than that of CoHCF-B after the system returns to the stable open circuit voltage; thus, it can be suggested that CoHCF-R maintains a more complete framework structure to allow more Na^+ ions to move back into the open sites than CoHCF-B after cycling.

The Fourier transform infrared spectroscopy (FT-IR) results shown in Fig. 5 further demonstrate the difference between CoHCF-B and CoHCF-R in the framework structure after cycling. The strongest absorption peak at the wavenumber of 2073 cm^{-1} and a weaker peak at 596 cm^{-1} are associated with the stretching vibrations of cyanide (ν(C≡N) and ν(Fe–CN)) in $[Fe(CN)_6]$ ligands.[33] It also can be observed that the weak absorption peak of hydroxyl at 1616 cm^{-1} indicates a small amount of water molecules in the materials. To quantitatively analyse the intensity of the characteristic absorption peaks, the relative intensities I_t (as shown in Fig. S5†) of ν(C≡N) and ν(Fe–CN) were calculated, and further calculations of the ratio of ν(Fe–CN)/ν(C≡N) were carried out to study the change in structure. The specific values of I_t ratio of ν(Fe–CN)/ν(C≡N) for CoHCF-B and CoHCF-R before (1, 2) and after (3, 4) cycling are 0.91, 0.9, 0.8, and 0.88, respectively, which indicate the relatively weak stretching vibration of ν(Fe–CN) in CoHCF-B after cycling. It can be suggested that the degradation of the framework causes decrease in the relative amount of Fe–CN in $[Fe(CN)_6]$ ligands. At the same time, it should be noticed that the position of the absorption peak has a significant blue-shift, which

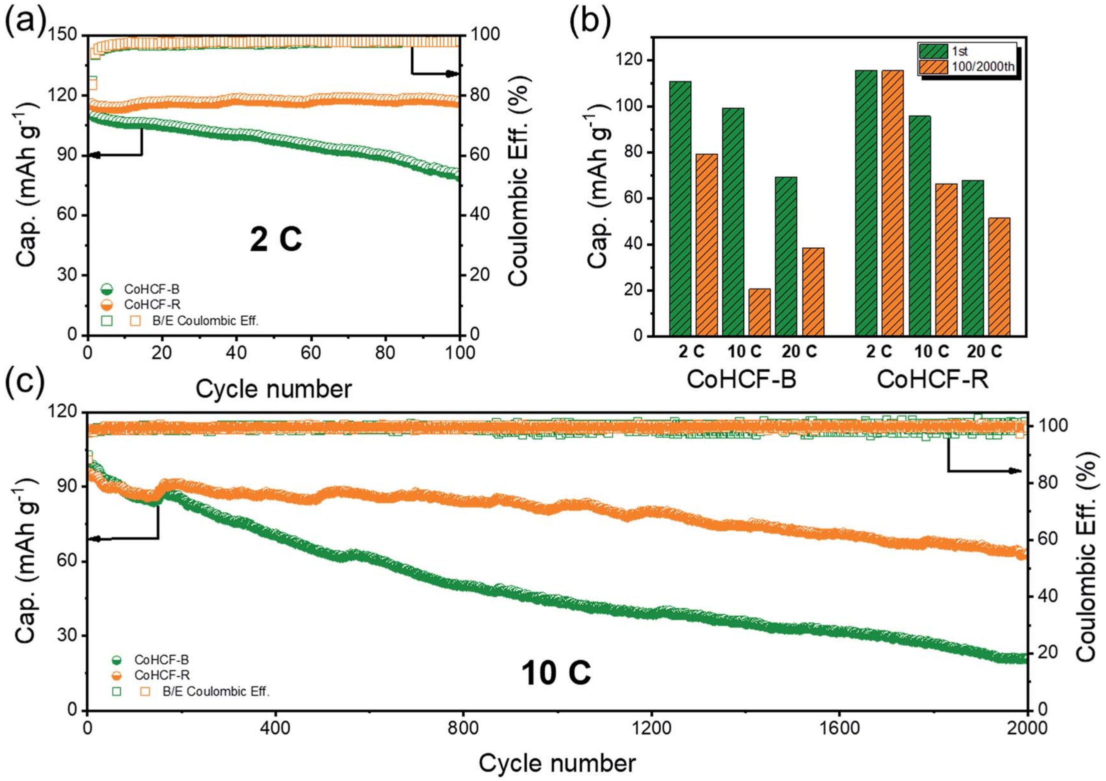

Fig. 3 (a) and (c) Cycle performances of CoHCF-B and CoHCF-R at current densities of 2C/10C/20C (Fig. S2†). (b) Comparison of discharge capacities at 1st, 100th, 2000th cycle of CoHCF-B and CoHCF-R.

is related to the changes in the coordination environment that are caused by the redox reaction of the nitrogen-coordinated Co^{3+}/Co^{2+} couple.[10] Both the ratio change and blue-shift results indicate the change of cyanide ligands in the framework structure.

Considering the dissolution of CoHCF in the aqueous electrolyte, the solubility equilibrium of CoHCF can be described by the following equation:

$$Na_2CoFe(CN)_{6(s)} \rightleftharpoons 2Na^+_{(aq)} + Co^{2+}_{(aq)} + [Fe(CN)_6]^{4-}_{(aq)} \quad (3)$$

Adding Co^{2+} ions can shift the dissolution equilibrium to the left and reduce the dissolution of CoHCF. Furthermore, adding Co^{2+} can make up for the dissolution of Co^{2+} ions, causing structural degradation and maintaining a stable structure. Inductively coupled plasma-atomic emission spectroscopy (ICP-AES) was employed to measure the Fe content in the electrolyte after 2000 cycles at a current density of 10C. The results of three parallel samples are shown in Fig. 6,

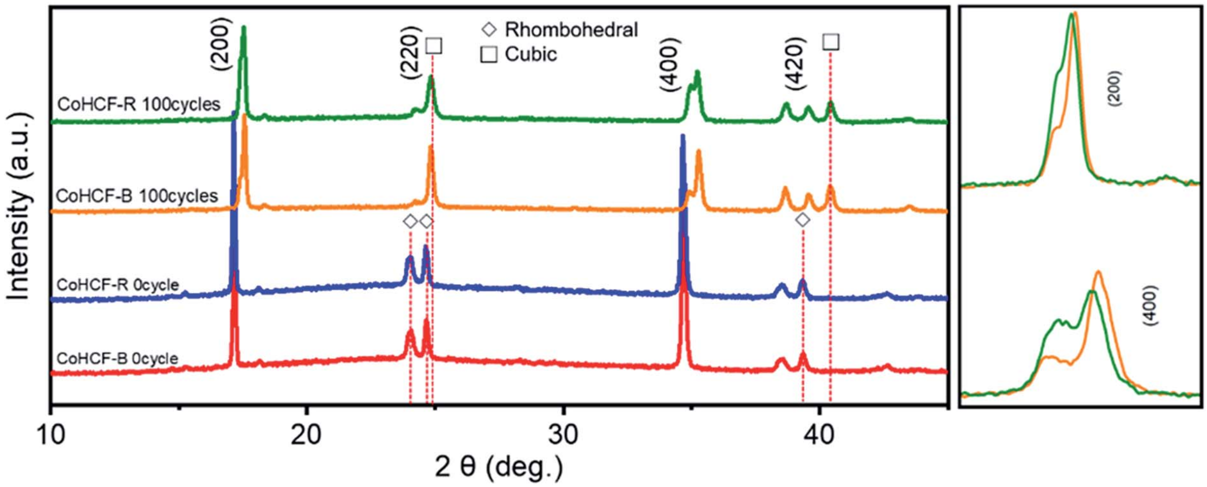

Fig. 4 XRD patterns of CoHCF-B and CoHCF-R before and after 100 cycles.

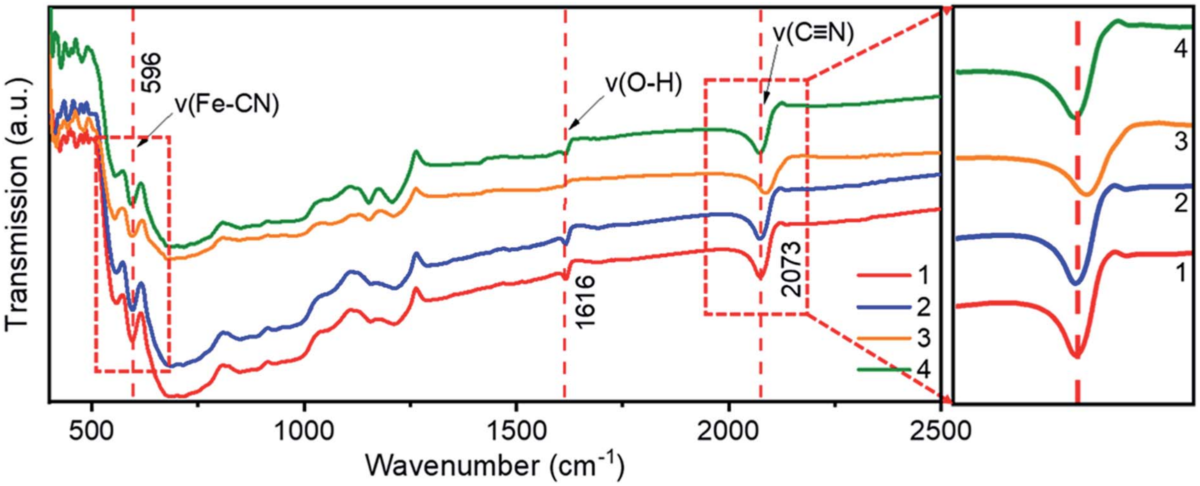

Fig. 5 FT-IR spectra of CoHCF-B and CoHCF-R before (1, 2) and after (3, 4) 100 cycles.

which indicate that the Fe content in CoHCF-R is much lower than that in CoHCF-B. The result also proves that the framework structure of CoHCF is conserved better after adding Co^{2+} ions. The average Fe contents are 4.19 mg L^{-1} for CoHCF-B and 1.35 mg L^{-1} for CoHCF-R in the electrolytes. Considering the volume of aqueous electrolyte (30 mL) and the average active material weight (~2.5 mg), ~30% and ~10% of the active material (CoHCF) are decomposed or dissolved from the framework structure for CoHCF-B and CoHCF-R, which correspond to the cycle performances of the two samples. So far, all results demonstrate that the framework structure is maintained by the added Co^{2+} ions, and it may act to stabilize the M_1–N≡C–Fe bridge, reducing the degradation of the framework structure during cycling. On the other hand, the increase in the concentration of Co^{2+} ions in the electrolyte also helps to inhibit continuous dissolution of CoHCF.

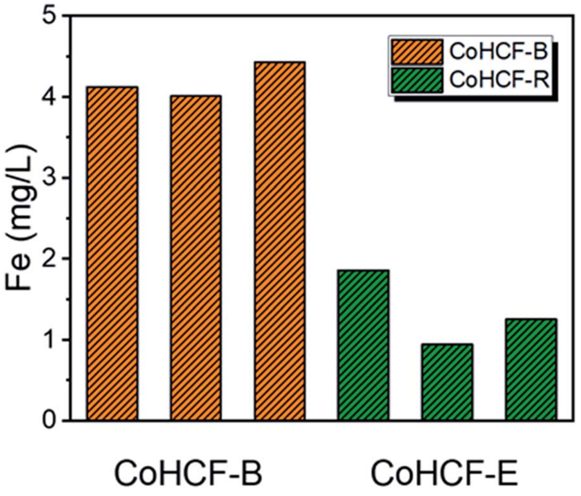

Fig. 6 Comparison of Fe contents in electrolyte after 2000 cycles of CoHCF-B and CoHCF-R.

Conclusions

In this study, we synthesized highly crystalline Prussian blue CoHCF nanocubes (~500 nm) with sharp edges and flat surfaces by using an optimized and facile coprecipitation method. By adding an electrolyte additive (1 wt% $CoSO_4$) in the aqueous electrolyte, the cycle performance was significantly improved. The capacity retentions increased from 71.5%, 20.8%, and 55.7% to 100%, 69.2%, and 75.6%, respectively. After the addition of Co^{2+} ions at different current densities and cycling numbers, the XRD and FT-IR results demonstrated that the framework structure of CoHCF is maintained during the insertion/extraction process of Na^+ ions after adding Co^{2+} ions, and the ICP results show that the degradation and dissolution of the CoHCF framework structure significantly decrease. Our results demonstrate that adding electrolyte additives can restrain the PBA framework structure from collapse and dissolution; this study can guide further improvement in the overall electrochemical performances of the PBA electrodes in ASIBs.

Conflicts of interest

There are no conflicts to declare.

Acknowledgements

This work was supported by the Shenzhen Science and Technology Research Grant (JCYJ20170412150450297) and the National Natural Science Foundation of China (21622407, 21875266).

Notes and references

1 J. Chen, *Materials*, 2013, **6**, 156–183.
2 K. Zaghib, A. Mauger, H. Groult, J. B. Goodenough and C. M. Julien, *Materials*, 2013, **6**, 1028–1049.

3 X. S. Wang, K. Z. Du, C. Wang, L. X. Ma, B. L. Zhao, J. F. Yang, M. X. Li, X. X. Zhang, M. Q. Xue and J. T. Chen, *ACS Appl. Mater. Interfaces*, 2017, **9**, 38606–38611.

4 K. Kubota, M. Dahbi, T. Hosaka, S. Kumakura and S. Komaba, *Chem. Rec.*, 2018, **18**, 459–479.

5 L. X. Zhang, X. S. Wang, W. J. Deng, X. L. Zang, C. Y. Liu, C. Li, J. T. Chen, M. Q. Xue, R. Li and F. Pan, *Nanoscale*, 2018, **10**, 958–963.

6 X. S. Wang, Z. H. Yang, C. Wang, L. X. Ma, C. S. Zhao, J. T. Chen, X. X. Zhang and M. Q. Xue, *Nanoscale*, 2018, **10**, 800–806.

7 M. I. Jamesh and A. S. Prakash, *J. Power Sources*, 2018, **378**, 268–300.

8 H. Zhang, S. Jeong, B. Qin, D. Vieira Carvalho, D. Buchholz and S. Passerini, *ChemSusChem*, 2018, **11**, 1382–1389.

9 Q. Yang, W. Wang, H. Li, J. Zhang, F. Kang and B. Li, *Electrochim. Acta*, 2018, **270**, 96–103.

10 W. Li, F. Zhang, X. Xiang and X. Zhang, *J. Phys. Chem. C*, 2017, **121**, 27805–27812.

11 M. A. Oliver-Tolentino, J. Vázquez-Samperio, S. N. Arellano-Ahumada, A. Guzmán-Vargas, D. Ramírez-Rosales, J. A. Wang and E. Reguera, *J. Phys. Chem. C*, 2018, **122**, 20602–20610.

12 X. Wu, M. Sun, S. Guo, J. Qian, Y. Liu, Y. Cao, X. Ai and H. Yang, *ChemNanoMat*, 2015, **1**, 188–193.

13 C. Y. Liu, X. S. Wang, W. J. Deng, C. Li, J. T. Chen, M. Q. Xue, R. Li and F. Pan, *Angew. Chem., Int. Ed.*, 2018, **57**, 7046–7050.

14 Y. You, X.-L. Wu, Y.-X. Yin and Y.-G. Guo, *Energy Environ. Sci.*, 2014, **7**, 1643–1647.

15 X. Wu, C. Wu, C. Wei, L. Hu, J. Qian, Y. Cao, X. Ai, J. Wang and H. Yang, *ACS Appl. Mater. Interfaces*, 2016, **8**, 5393–5399.

16 L. Wang, Y. Lu, J. Liu, M. Xu, J. Cheng, D. Zhang and J. B. Goodenough, *Angew. Chem., Int. Ed.*, 2013, **52**, 1964–1967.

17 Y. Moritomo, K. Igarashi, T. Matsuda and J. Kim, *J. Phys. Soc. Jpn.*, 2009, **78**, 074602-1–074602-4.

18 M. Pasta, R. Y. Wang, R. Ruffo, R. Qiao, H.-W. Lee, B. Shyam, M. Guo, Y. Wang, L. A. Wray, W. Yang, M. F. Toney and Y. Cui, *J. Mater. Chem. A*, 2016, **4**, 4211–4223.

19 X. Bie, K. Kubota, T. Hosaka, K. Chihara and S. Komaba, *J. Power Sources*, 2018, **378**, 322–330.

20 Y. You, H. R. Yao, S. Xin, Y. X. Yin, T. T. Zuo, C. P. Yang, Y. G. Guo, Y. Cui, L. J. Wan and J. B. Goodenough, *Adv. Mater.*, 2016, **28**, 7243–7248.

21 Y. T. Peng, Z. Y. Le, M. C. Wen, D. Q. Zhang, Z. Chen, H. B. Wu, H. X. Li and Y. F. Lu, *Nano Energy*, 2017, **35**, 44–51.

22 Y. Jiang, S. Yu, B. Wang, Y. Li, W. Sun, Y. Lu, M. Yan, B. Song and S. Dou, *Adv. Funct. Mater.*, 2016, **26**, 5315–5321.

23 C. Li, X. Wang, W. Deng, C. Liu, J. Chen, R. Li and M. Xue, *ChemElectroChem*, 2018, **5**, 3887–3892.

24 C. Li, R. Zang, P. Li, Z. Man, S. Wang, X. Li, Y. Wu, S. Liu and G. Wang, *Chem.–Asian J.*, 2018, **13**, 342–349.

25 C. D. Wessells, M. T. McDowell, S. V. Peddada, M. Pasta, R. A. Huggins and Y. Cui, *ACS Nano*, 2012, **6**, 1688–1694.

26 N. Sattarahmady, H. Heli and S. E. Moradi, *Sens. Actuators, B*, 2013, **177**, 1098–1106.

27 P. Nie, J. Yuan, J. Wang, Z. Le, G. Xu, L. Hao, G. Pang, Y. Wu, H. Dou, X. Yan and X. Zhang, *ACS Appl. Mater. Interfaces*, 2017, **9**, 20306–20312.

28 Z. Le, F. Liu, P. Nie, X. Li, X. Liu, Z. Bian, G. Chen, H. B. Wu and Y. Lu, *ACS Nano*, 2017, **11**, 2952–2960.

29 H. Li, X. Yu, Y. Bai, F. Wu, C. Wu, L.-Y. Liu and X.-Q. Yang, *J. Mater. Chem. A*, 2015, **3**, 9578–9586.

30 L. Wu, Y. Hu, X. Zhang, J. Liu, X. Zhu and S. Zhong, *J. Power Sources*, 2018, **374**, 40–47.

31 C. Chen, Y. Dong, S. Li, Z. Jiang, Y. Wang, L. Jiao and H. Yuan, *J. Power Sources*, 2016, **320**, 20–27.

32 X. Wu, Y. Luo, M. Sun, J. Qian, Y. Cao, X. Ai and H. Yang, *Nano Energy*, 2015, **13**, 117–123.

33 Y. Huang, M. Xie, J. Zhang, Z. Wang, Y. Jiang, G. Xiao, S. Li, L. Li, F. Wu and R. Chen, *Nano Energy*, 2017, **39**, 273–283.

34 X. Yan, Y. Yang, E. Liu, L. Sun, H. Wang, X.-Z. Liao, Y. He and Z.-F. Ma, *Electrochim. Acta*, 2017, **225**, 235–242.

35 H. C. Gao, S. Xin, L. G. Xue and J. B. Goodenough, *Chem*, 2018, **4**, 833–844.

36 X. Y. Wu, Y. L. Cao, X. P. Ai, J. F. Qian and H. X. Yang, *Electrochem. Commun.*, 2013, **31**, 145–148.

37 H. Gao, L. Xue, S. Xin, K. Park and J. B. Goodenough, *Angew. Chem., Int. Ed.*, 2017, **56**, 5541–5545.